Letter

Vol. 50, No. 16/15 August 2025/*Optics Letters* 5077

Optics Letters

Non-iterative distortion correction for Scheimpflug multi-view microscopic fringe projection profilometry

SUDONG DING,[1,2,†] ZIQIANG WEI,[1,2,†] YAN HU,[1,2,*] WENHUI LI,[3] SHICHAO GAO,[1,2] LIQI ZHANG,[1,2] QIAN CHEN,[2,4] AND CHAO ZUO[1,2,5]

[1] *Smart Computational Imaging Laboratory (SCILab), Nanjing University of Science and Technology, Nanjing, Jiangsu 210094, China*
[2] *Jiangsu Key Laboratory of Visual Sensing & Intelligent Perception, Nanjing, Jiangsu 210094, China*
[3] *Konfoong Biotech International Company Ltd., Ningbo, Zhejiang 315499, China*
[4] *chenqian@njust.edu.cn*
[5] *zuochao@njust.edu.cn*
[†] *These authors contributed equally to this work.*
**hu_yan@njust.edu.cn*

Received 21 May 2025; revised 4 July 2025; accepted 14 July 2025; posted 17 July 2025; published 11 August 2025

Microscopic fringe projection profilometry (MFPP) has become an essential technique for precisely inspecting intricate microscale industrial parts, where Scheimpflug multi-view imaging is commonly used to extend the depth of field (DOF). However, lens distortion significantly reduces measurement accuracy, creating a major challenge for seamlessly fusing data from different views. In this Letter, we introduce a non-iterative distortion correction method for Scheimpflug multi-view MFPP that directly remaps camera and projector pixels using pre-calibrated parameters. The undistorted position for unidirectional fringes is calculated by intersecting undistorted camera sight lines with a sub-pixel-interpolated DMD grid, thereby eliminating the need for pattern reloading or iterative optimization. Experiments with a dual Scheimpflug camera MFPP system show that the proposed approach decreases the root-mean-square error (RMSE) of 3D measurements for planes and standard spheres by 43.5% and 21.1%, respectively. Additionally, reconstructing a complex aircraft model demonstrates the method's ability for seamless multi-view fusion, providing a computationally efficient and accurate solution for micro-scale 3D metrology.

https://doi.org/10.1364/OL.568062

Introduction. Fringe projection profilometry (FPP) is a non-contact 3D measurement method with a significant potential in industrial inspection, reverse engineering, and robotic vision [1–3], because of its micron-level precision, full-field imaging capability, and high-resolution [4,5], while recent variants such as parallel single-pixel imaging are further improving its robustness under complex illumination [6,7]. However, traditional FPP systems struggle to balance accuracy with field of view (FOV) when measuring miniaturized objects [8]. Micro-scale fringe projection profilometry addresses this issue by combining fringe projection with well-calibrated microscopic optical paths to achieve sub-micron measurement accuracy [9]. To further enhance measurement capabilities, multi-view 3D data acquisition and fusion are employed to mitigate occlusion and expand the viewing range for industrial parts with 3D complex structures [10–12]. In multi-view micro-scale systems, the Scheimpflug principle extends the DOF by tilting the lens and sensor planes, maintaining high image sharpness across all views and enabling high-precision measurements of complex parts across a substantial volume [13]. Building upon the Scheimpflug principle to extend the DOF, researchers have been developing ways to address the calibration accuracy of such systems. Sun *et al.* comprehensively reviewed the calibration methods for Scheimpflug cameras and analyzed the performance of mainstream calibration models [14], providing a solid theoretical foundation for choosing an appropriate calibration model to optimize measurement accuracy. Deng *et al.* proposed an accurate and flexible calibration method for a 3D microscopic structured light system, enhancing measurement precision by optimizing the sub-pixel correspondence between a Scheimpflug projector and camera [15]. However, in micro-scale 3D measurement, the inherent nonlinear distortions of lenses can significantly affect measurement accuracy and hinder precise multi-view data fusion. To address this, researchers have conducted extensive studies in lens distortion-correction. Li *et al.* [16] improved measurement accuracy by generating pre-distorted fringe patterns based on the projector's lens model; however, the need to individually pre-process and reload each pattern introduces considerable computational complexity. Zhang *et al.* [17] proposed a real-time scale-offset model to dynamically compensate for projection distortion, although its effectiveness may be limited in complex scenarios with diverse distortion types. Yang *et al.* [18] proposed a residual compensation method that refines the distortion map to address remaining lens errors, but it can be computationally expensive for high-resolution data. These methods, while effective in specific contexts, may fall short in addressing the distortions, potentially leading to insufficient accuracy for Scheimpflug multi-view systems.

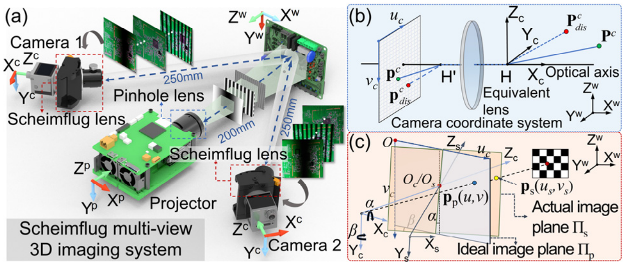

Fig. 1. (a) The structure diagram of the Scheimpflug multi-view 3D imaging system. (b) Pinhole camera model with distortion. (c) The model of the camera sensor's Scheimpflug angle.

In this Letter, we propose an efficient, non-iterative distortion-correction method that utilizes the pre-calibrated camera and projector parameters, achieving high accuracy with only unidirectional fringe patterns. The Scheimpflug multi-view fringe projection system (Fig. 1(a)) comprises a digital projector and two industrial cameras with Scheimpflug lenses. The classic pinhole camera model in Fig. 1(b) maps the 3D scene points to a 2D sensor plane via a linear projection in Eq. (1):

$$s\begin{bmatrix} u \\ v \\ 1 \end{bmatrix} = \underbrace{\begin{bmatrix} f_x & 0 & u_0 \\ 0 & f_y & v_0 \\ 0 & 0 & 1 \end{bmatrix}}_{\mathbf{A}} \underbrace{\begin{bmatrix} r_{11} & r_{12} & r_{13} & t_x \\ r_{21} & r_{22} & r_{23} & t_y \\ r_{31} & r_{32} & r_{33} & t_z \end{bmatrix}}_{\mathbf{R}|\mathbf{T}} \begin{bmatrix} X_w \\ Y_w \\ Z_w \\ 1 \end{bmatrix}. \tag{1}$$

Here, s denotes the perspective factor, $\mathbf{A}$ illustrates the camera's intrinsic parameters, $\mathbf{R}$ represents the rotation vectors, and $\mathbf{T}$ is a translation vector.

As shown in Fig. 1(c), to model the imaging of a pinhole camera under Scheimpflug conditions, we assume a virtual sensor perpendicular to the optical axis, which is obtained by rotating the actual sensor around its intersection with the optical axis by angles α and β around the horizontal and vertical axes in the camera coordinate space. The initial intersection point position is obtained by using the standard pinhole model. However, the corresponding focal length will also vary due to the choice of principal point location. Therefore, the distortion must be combined with all parameters for overall optimization. The model can derive the precise mapping relationship between the point $\tilde{\mathbf{p}}_s$ $[u_s\ v_s\ 1]^T$ on the actual sensor plane and the point $\tilde{\mathbf{p}}_p$ $[u\ v\ 1]^T$ on the virtual sensor plane, as detailed in Eqs. (2) and (3):

$$\tilde{\mathbf{p}}_s = \mathbf{R}_S(\alpha,\beta)\,\mathbf{K}(\alpha,\beta)\,\tilde{\mathbf{p}}_p. \tag{2}$$

Here, $\mathbf{R}_S\,(\alpha,\beta)$ is the rotation matrix between the two planes, and $\mathbf{K}\,(\alpha,\beta)$ represents the coordinate scaling transformation matrix caused by the perspective projection between them.

$$\begin{cases} \mathbf{K}(\alpha,\beta) = \begin{bmatrix} \cos\alpha\cos\beta & 0 & \cos\alpha\sin\beta \\ 0 & \cos\alpha\cos\beta & -\sin\alpha \\ 0 & 0 & 1 \end{bmatrix} \\ \mathbf{R}_S(\alpha,\beta) = \begin{bmatrix} \cos\beta & \sin\alpha\sin\beta & -\cos\alpha\sin\beta \\ 0 & \cos\alpha & \sin\alpha \\ \sin\beta & -\sin\alpha\cos\beta & \cos\alpha\cos\beta \end{bmatrix} \end{cases} \tag{3}$$

As depicted in Fig. 2, lens distortion causes the object point $\mathbf{P}(X_u^w, Y_u^w, Z_u^w)$ to be mapped to the distorted points $\mathbf{p}^c_{dis}(u^c_d, v^c_d)$ and $\mathbf{p}^p_{dis}(u^p_d, v^p_d)$ on the camera's CMOS pixel plane and projector's DMD pixel plane, respectively. Under ideal undistorted conditions, these points should map to the pixel points $\mathbf{p}^c(u^c_u, v^c_u)$ and $\mathbf{p}^p(u^p_u, v^p_u)$. Therefore, in practice, we measure points with errors, resulting in a deviated 3D point $\mathbf{P}'$. For the projector, radial distortion k_1, k_2, and tangential distortions p_1 and p_2 must be considered. In contrast, for the Scheimpflug camera, tangential distortion is already incorporated into the Scheimpflug angles, so it does not need to be modeled again in the distortion, as the sensor tilt inherently accounts for this distortion. In the 3D measurement, we first calculate the undistorted 3D data obtained from the two cameras working with the projector separately and then fuse them to achieve a complete 3D data. The flowchart of the proposed method is shown in Fig. 3, which summarizes the five steps as follows:

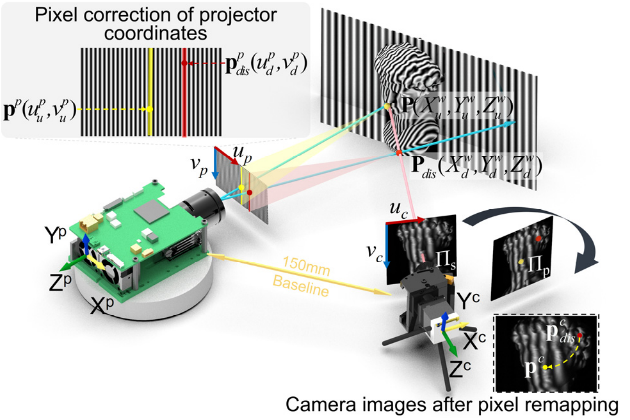

Fig. 2. The schematic of the projector distortion model using unidirectional fringe patterns.

Step 1: Based on the multi-view Scheimpflug system, we synchronize the cameras to capture the encoded fringe images and calculate the unwrapped phase maps. For calibration, we establish a one-to-one correspondence between control points on the object side and the DMD or CMOS plane.

Step 2: The cameras are calibrated using the Scheimpflug model, and the projector is calibrated using the pinhole model. To improve the calibration accuracy, the reprojection errors of both cameras and projectors are optimized globally, considering the distortion, using the Levenberg–Marquardt algorithm [15].

Step 3: Leveraging the calibrated camera parameters, the distortion offset initially expressed on the camera's normalized plane is remapped into the virtual sensor plane by Eq. (2). In the distorted image, the remapping causes each pixel's coordinates to become elements in an array, indexed by the coordinate values. For the projector, the remapping is also conducted. However, the projector's coordinates are obtained indirectly, so distortion elimination requires the assistance of calibrated cameras, which are introduced in the next step.

Step 4: Using the established remapping relation, we have the corrected camera rays, marked as the sight line in Fig. 3, which is expressed by a linear equation. For each camera pixel, the phase value on its line helps determine an initial distorted 3D point based on the established triangulation. Then, the 3D data are inversely mapped on the DMD to locate an exact point instead of a line corresponding to the phase value. Since unidirectional fringe patterns determine a unique 3D point, fringe patterns in other directions can be discarded to improve the efficiency. Based on the pixel remapping relation established in the last step, we can find the undistorted DMD position.

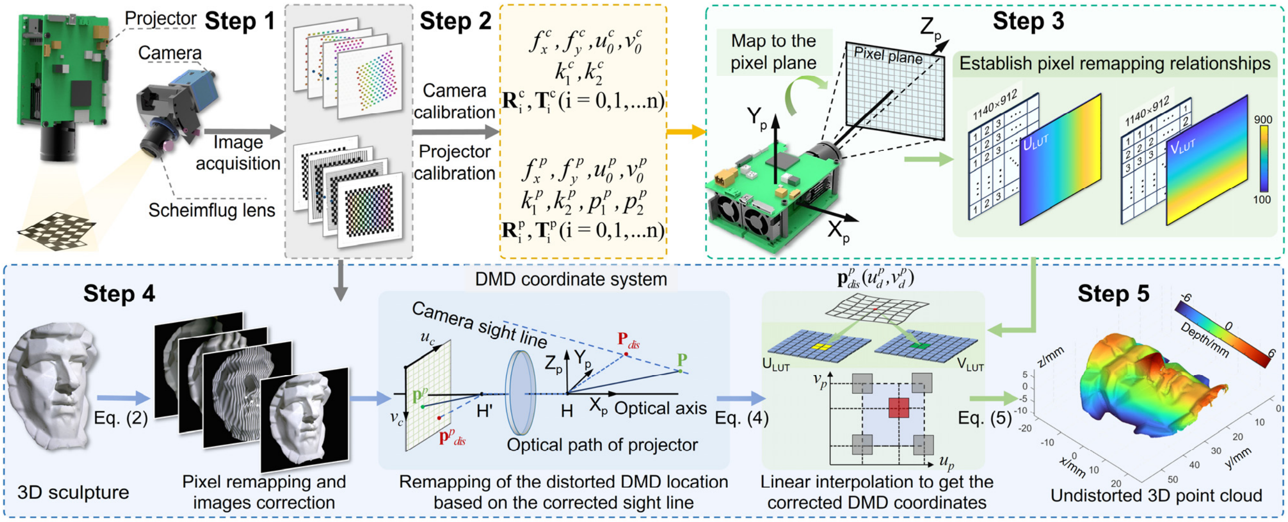

Fig. 3. The flowchart of the proposed non-iterative distortion-correction method for 3D measurement using the Scheimpflug imaging.

Table 1. Calibrated Results of the Projector and Cameras

	Camera 1	Camera 2	Projector
k_1, k_2	[0.031 –0.410]	[0.038 –0.692]	[0.110 –1.434]
p_1, p_2	-	-	[0.006 0.004]
α, β (°)	[0.367 2.800]	[0.311 –3.398]	-
A	$\begin{bmatrix} 9103 & 0 & 483.5 \\ 0 & 9151 & 718.4 \\ 0 & 0 & 1 \end{bmatrix}$	$\begin{bmatrix} 9168 & 0 & 1468 \\ 0 & 9051 & 710.0 \\ 0 & 0 & 1 \end{bmatrix}$	$\begin{bmatrix} 3533 & 0 & 431.2 \\ 0 & 9167 & 600.1 \\ 0 & 0 & 1 \end{bmatrix}$
$\mathbf{R_v}$	[0.088 –0.521 0.042]	[0.071 0.511 –0.029]	[0.058 0.007 –0.011]
T	[–24.16 –12.60 274.6]	[2.372 –10.35 291.3]	[–12.29 –12.50 266.2]

Step 5: Since the remapped coordinates are typically non-integer, interpolation is necessary to complete the transformation for both the camera and projector. For the camera, the bilinear interpolation is applied at the remapped coordinates to obtain the intensity values for accurate phase calculation. For the projector, the distorted 3D point $\mathbf{P}_{dis}(X_d^w, Y_d^w, Z_d^w)$ is first mapped back to a pixel position $\mathbf{p}_{dis}(u_d^p, v_d^p)$ and then interpolated to obtain the corrected position $\mathbf{p}^p(u_u^p, v_u^p)$ by:

$$\begin{cases} u_u^p = \mathrm{Interp}(U_{LUT}^P, u_d^p, v_d^p) \\ v_u^p = \mathrm{Interp}(V_{LUT}^P, u_d^p, v_d^p) \end{cases}. \tag{4}$$

Here, U_{LUT}^P and V_{LUT}^P are the look up table of the remapping relation of the projector's pixel coordinates. The resulting undistorted coordinates are then used to linearly reconstruct the corrected 3D point $\mathbf{P}(X_u^w, Y_u^w, Z_u^w)$ through:

$$\begin{bmatrix} X_u^w \\ Y_u^w \\ Z_u^w \end{bmatrix} = \begin{bmatrix} p_{11}^c - p_{31}^c u_u^c & p_{12}^c - p_{32}^c u_u^c & p_{13}^c - p_{33}^c u_u^c \\ p_{21}^c - p_{31}^c v_u^c & p_{22}^c - p_{32}^c v_u^c & p_{23}^c - p_{33}^c v_u^c \\ p_{11}^p - p_{31}^c u_u^p & p_{21}^p - p_{32}^c u_u^p & p_{31}^p - p_{33}^c u_u^p \end{bmatrix}^{-1} \times \begin{bmatrix} p_{14}^c - p_{34}^c u_u^c \\ p_{24}^c - p_{34}^c v_u^c \\ p_{14}^p - p_{34}^c u_u^p \end{bmatrix}. \tag{5}$$

The 3D measurement system comprises a DLP4500 projector (1140 × 912 pixels) and two Basler acA2040-120um cameras (2048 × 1536 pixels) with a 28 mm Opto-Engineering MCSM1-01X Scheimpflug lens. Using the standard phase-shifting algorithm, we projected fringe patterns at frequencies of (1, 7, 76) with phase shifts of (4, 4, 8) steps. The system calibration parameters are summarized in Table 1. The rotation matrix is transformed into a 3-element vector $\mathbf{R_v}$ through the Rodrigues transformation.

We validated our distortion-correction method by experiments on a planar surface and two standard spheres (Fig. 4). The initial reconstruction of the planar surface showed significant distortion (Figs. 4(a) and 4(b)), which was dramatically optimized after correction, with the RMSE decreasing from 38.8 and 31.3 μm to 14.6 and 23.6 μm of the two views, respectively (Figs. 4(c) and 4(d)). The measurements of spheres showed that our correction reduced the RMSE of sphere fitting from 9.5 and 10.1 μm to 7.0 and 8.5 μm of the two spheres, respectively (Fig. 4(e)). The corrected data yielded a diameter much closer to the true value, with a standard deviation of 6.2 μm across multiple measurements (Fig. 4(f)).

To verify the effectiveness of the proposed method in complex 3D scenarios, we performed measurements on an aircraft model with undulating and gully structures. The results are visually validated and quantitatively supported by the comparisons of depth curves (Fig. 5(a)), demonstrating the accurate capture of intricate geometric details. The multi-view point cloud fusion (Fig. 5(b)) successfully integrates surface details from two views, aided by the phase-guided Fast Point Feature Histogram (FPFH) registration method and Iterative Closest Point (ICP) refinement.

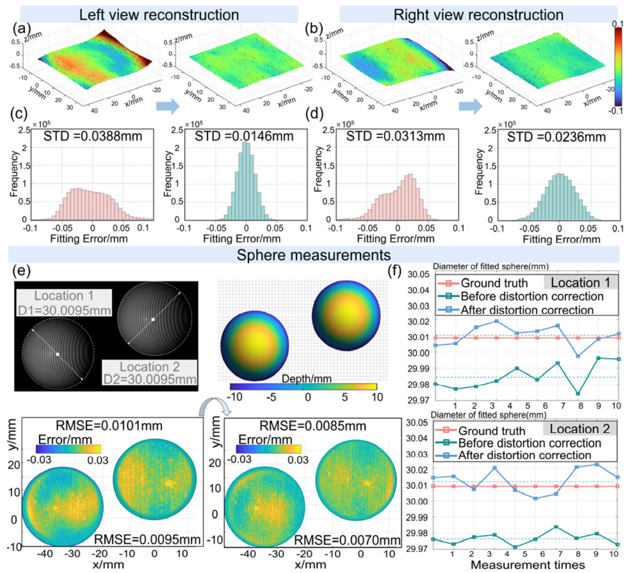

Fig. 4. The validation of the proposed method through comparative experiments involving a planar surface and standard spheres. (a), (b) 3D reconstruction of the plane from the left and right views. (c), (d) The statistics of the reconstructed height distribution. (e) 3D reconstruction of the spheres and error analysis. (f) The comparative results of the fitted diameter from multiple measurements.

The cross section of the fused data reveals a very high degree of overlap between the two views. The mean nearest-neighbor distance in the overlapping region of the registered point cloud drops from 36.9 μm before correction to 25.3 μm after correction, clearly demonstrating the effectiveness of our distortion correction method for Scheimpflug multi-view microscopic fringe projection profilometry.

In conclusion, this work presents a new non-iterative distortion-correction method for Scheimpflug multi-view systems, effectively reducing the negative impact of lens distortions on high-precision 3D measurements at the micro-scale. The main innovation of pixel coordinate remapping, combined with pre-calibrated parameters, allows for quick and efficient 3D reconstruction through linear calculations of only unidirectional fringe patterns, exceeding the capabilities of iterative methods and lowering the computational load for real-time use. Experimental results show significant improvements in accuracy for various surfaces, including those with complex details. Future research will aim to broaden applications to difficult industrial inspection scenarios, such as in-line quality control, and to integrate with complementary 3D imaging techniques.

Funding. National Key Research and Development Program of China (2022YFB2804603, 2024YFF0505600); Young Elite Scientists Sponsorship Program by CAST (2022QNRC001); National Natural Science Foundation of China (62005121); Fundamental Research Funds for the Central Universities (30924010814).

Disclosures. The authors declare no conflicts of interest.

Data availability. No data were generated or analyzed in the presented research.

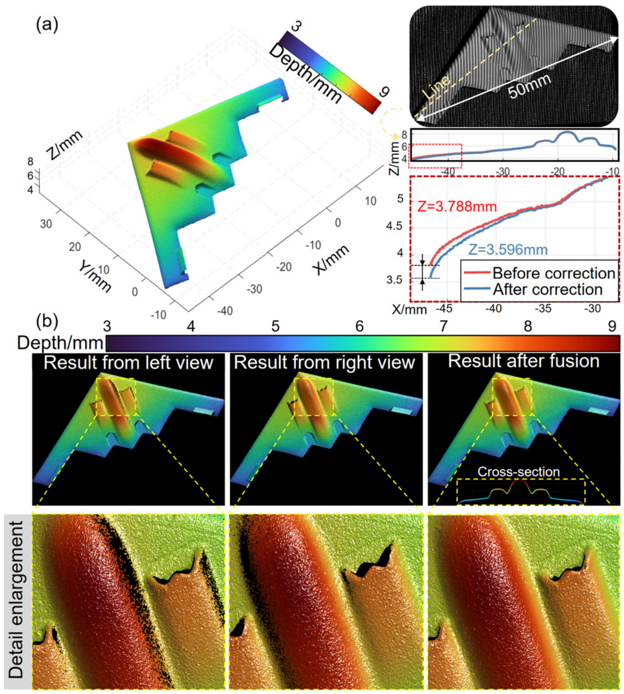

Fig. 5. The experiment of multi-view 3D measurement of an aircraft model. (a) The 3D reconstruction of the aircraft and the depth variation curve in the key area. (b) The point cloud from the left view, right view, and the fused point cloud.

REFERENCES

1. C. Zuo, L. Huang, M. Zhang, *et al.*, Opt. Lasers Eng. **85**, 84 (2016).
2. S. Feng, Q. Chen, G. Gu, *et al.*, Adv. Photon. **1**, 1 (2019).
3. J. Qian, Y. Cao, Y. Bi, *et al.*, eLight **3**, 4 (2023).
4. P. Yao, S. Gai, and F. Da, Opt. Lett. **46**, 4442 (2021).
5. W. Chen, S. Feng, W. Yin, *et al.*, PhotoniX **5**, 25 (2024).
6. Z. Wu, H. Wang, F. Chen, *et al.*, Light Adv. Manuf. **5**, 1 (2024).
7. F. Chen, Y. Shen, C. Liu, *et al.*, "Modeling of Parallel Single-Pixel Imaging for 3D Reconstruction: New Insights and Opportunities," (2025).
8. P. Shanmugam and K. Falaggis, Appl. Opt. **62**, 8334 (2023).
9. Y. Hu, Q. Chen, S. Feng, *et al.*, Opt. Lasers Eng. **135**, 106192 (2020).
10. R. Dai, W. Li, and Y.-H. Liu, IEEE Trans. Image Proc. **34**, 2124 (2025).
11. G. Zhang, Y. Liu, Q. Yao, *et al.*, Opt. Express **32**, 19146 (2024).
12. H. Deng, Y. Liu, G. Zhang, *et al.*, Measurement **222**, 113609 (2023).
13. M. Wang, Y. Yin, D. Deng, *et al.*, Opt. Express **25**, 19408 (2017).
14. C. Sun, H. Liu, M. Jia, *et al.*, J. Sens. **2018**, 1 (2018).
15. H. Deng, P. Hu, G. Zhang, *et al.*, Opt. Express **31**, 3092 (2023).
16. K. Li, J. Bu, and D. Zhang, Opt. Lasers Eng. **85**, 53 (2016).
17. G. Zhang, B. Xu, D. L. Lau, *et al.*, Opt. Express **30**, 24507 (2022).
18. S. Yang, M. Liu, J. Song, *et al.*, Opt. Lasers Eng. **114**, 104 (2019).